Efficient removal of Cr(VI) contaminant using recoverable silica from volcanic ash as natural adsorbent: Synthesis and activity in the mechanism and kinetic adsorption

Early Zahwa Alharissa, Yuanita Efhiliana, Roto Roto, Mudasir Mudasir, Endang Tri Wahyuni *

Chemistry Department, Faculty of Mathematic and Natural Sciences, Gadjah Mada University, Sekip Utara PO. Box Bls 21, Yogyakarta, 55281, Indonesia

A B S T R A C T

Modification of silica purified from the Merapi volcanic ash with magnetic material of Fe_3O_4 and attachment of cetyl triamine bromide (CTA-Br) on the magnetic cored has been performed to provide recoverable and positive surfaced of natural adsorbent. The magnetic cored was prepared via co-precipitation and CTA-Br attachment was conducted by a facile strategy. Then, the modified adsorbents were characterized by SEM, TEM, XRD, and FTIR instruments and examined for removing anionic Cr(VI) from the water media. The characterization data confirmed that crystals of Fe_3O_4 coated by SiO_2 that has been bound with CTA-Br have been successfully formed. Additionally, increasing CTA-Br loaded gives thicker lamination on $Fe_3O_4@SiO_2/CTA$-Br, but the CTA-Br loaded with higher than 0.25 mmol, leads to the coating peeled out. It is also demonstrated that $Fe_3O_4@SiO_2/CTA$-Br prepared with CTA-Br 0.25 mmol is ideal for Cr(VI) anionic removal, regarding to the highest adsorption and very good separation or recovery process. Moreover, the optimal dose of $Fe_3O_4@SiO_2/CTA$-Br in the Cr(VI) removal was observed at 0.25 g/20 mL under condition of pH 3 for 60 min. The adsorption of Cr(VI) well fits the Langmuir isotherm model with an adsorption capacity of 3.38 mg g^{-1} and is in a good agreement with pseudo-second order giving kinetic constant at 0.005 g mg^{-1} min^{-1}. Thus, it is clear that the natural adsorbent material with recoverable properties for more efficient and wider application of removal Cr(VI) contaminant was expected from this study.

1. Introduction

Chromium element is found in two forms that are trivalent Cr(III) and hexavalent chromium Cr(VI) with very different properties. Trivalent chromium, Cr(III) in the aqueous solution exists as cationic form that is useful for maintaining the glucose concentration in human body [1] while Cr(VI) is found as anionic with high toxicity [2]. Therefore, the environmental contamination by Cr(VI) anion has become a major concern in around the world. The main sources of Cr(VI) anion contaminant are waste waters from mining, metal plating, tannery, pigment and paint manufactures, and pharmaceuticals [3,4]. It has been known that the existence Cr(VI) in water is feasible due to the more soluble and mobile character of the anion, thus it is easy to enter the tissues of living organism [5]. The effects

---

of Cr(VI) on human health are found to be toxic and carcinogenic [6,7]. It also affects chronic diseases in several parts such as kidney, skin, liver, and nervous system [3]. Hence, removing Cr(VI) anion is a primordial issue for researchers, especially in the recent decades of environmental chemistry [8].

Several methods to minimize concentration level of Cr(VI) anionic in wastewater have been reported that include photocatalytic reduction [9,10], precipitation [11,12], and adsorption [6,13]. Among them, adsorption has been shown as an alternative economic-less and efficient method for removal of metal ions [14–16]. Cost is an important parameter in comparing adsorbent materials. The low-cost adsorbent can be obtained from nature such as plant wastes resources [8], zeolite [17,18], clay [19], and from solid waste of fly ash [20]. The natural resource of adsorbents is not used in their raw state, but need treatment to enhance their adsorption capacity by creating new active sites to increase the effectivity of adsorption process. Additional treatment might be performed by modify the surface based on chemicals and physical agents [4]. Such natural adsorbents have been modified with cetyl triamine bromide (CTA-Br) to form positive charge surface [21]. The modification has to be carried out, because the unmodified zeolite, clay, and fly ash have negative charge surface originated from SiO_2 as main component, that cannot be used for adsorption of Cr(VI) anionic. By attaching CTA-Br into the silica, the silica surface become positive charged due to the presence of the protonated amine [22].

In addition to natural zeolite, clay, and fly ash, the priceless silica gel purified from volcanic ash has also been modified with CTA-Br, which showed an effective adsorbent to reduce anionic heavy metal contaminants [23]. Volcanic ash is results from volcano eruption [24], frequently occurring in active volcanoes found in many countries, including in Mt. Merapi Indonesia. This ash refers to the fine fragment below 2 mm of pyroclastic materials containing abundant mineral oxide. It may concern that volcanic ash is the main natural source of aluminosilicate with high surface characteristics that may be utilized for various purposes, including adsorbent [23, 25]. Therefore, using silica from volcanic ash solid waste is interesting in both regards to environmental and functional materials.

Furthermore, in the post of the adsorption process, the recovery of the adsorbent is usually carried out by impractical separation such as filtration using filter paper, which takes more time [26,27]. To overcome the impractical separation, coating the adsorbents [28,29] and TiO_2 photocatalysts [30,31] with a magnetic material such as Fe_3O_4 have been intensively studied. The separation of adsorbent can be conducted very fast and practically by contacting the adsorbent with external magnetic rode [32]. So far magnetic core-cell silica-based adsorbent from volcanic ash for removal of anionic Cr(VI) contaminant also has not been explored yet. The fast separation of the adsorbent after playing the role may enhance efficiency the whole system of adsorption process for upscale applications.

This research deals with the using of volcanic ash as a low-cost silica source, modified with CTA-Br to provide positive charge and magnetic Fe_3O_4 material contributing the recoverable property. The fabrication process to modify the natural adsorbent of volcanic ash is designed to use moderate conditions. Thus, it can be anticipated that the sustainable technique was implemented in this current research. Here, the influence of CTA-Br fraction in the adsorbent on the effectiveness of the anionic Cr(VI) removal is investigated. Besides, studies on the adsorbent having optimum CTA-Br loaded and the effects of the factors controlling the adsorption process are also provided. It is the strategic attempt to develop a material that came from nature with toxic repellent properties and good recoverability for an easier separation process. It may provide a circular system of sustainable chemistry to preserve the environment.
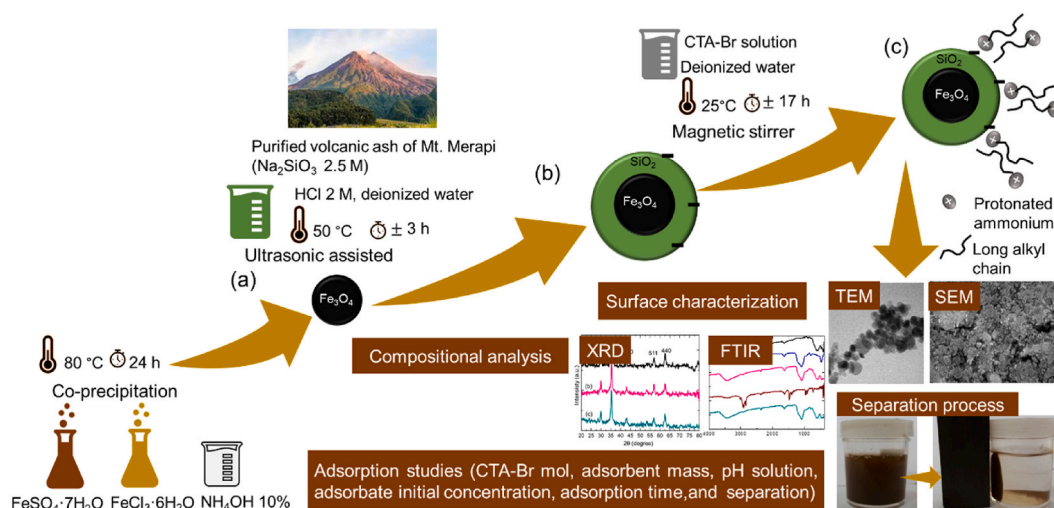
Scheme. 1. Pathway fabrication of the adsorbent from the base structure of (a) Fe_3O_4, (b) $Fe_3O_4@SiO_2$, and the final product of (c) $Fe_3O_4@SiO_2$/CTA-Br followed by the adsorbent characterization and adsorption assessments.

2. Materials and method

2.1. Materials

The silica source was obtained from Merapi volcanic ash and purified by existed method in Supplementary 1. $FeSO_4 \cdot 7H_2O$ and $FeCl_3 \cdot 6H_2O$ used to synthesize Fe_3O_4 as core adsorbent. HCl 37 %, NaOH, NH_4OH, $K_2Cr_2O_7$, and CTA-Br were purchased from Merck Co. Inc (Germany) without further purification. All solutions were prepared in distilled water.

2.2. Methods

The fabrication method for each step were illustrated in Scheme.1 which distinguish the three main synthesis concept Fe_3O_4 (Scheme.1a), $Fe_3O_4@SiO_2$ (Scheme.1b), and the final product of $Fe_3O_4@SiO_2/CTA-Br$ (Scheme.1c).

2.2.1. Preparation of Fe_3O_4

Synthesis of Fe_3O_4 using the co-precipitation method. The Fe_3O_4 was prepared from a solution containing of Fe(II) and Fe(III) with mol ratio 1:2, from the 8.1 g of $FeSO_4 \cdot 7H_2O$ and 4.2 g of $FeCl_3 \cdot 6H_2O$ with 60 mL deionized water. Into the solution, 60 mL of NH_4OH 10 % was added until the black sedimentation appeared. Then, the black solid was separated by filtration, then was rinsed by deionized water until the neutral pH was obtained, and was dried in an oven at 80 °C for about 24 h.

2.2.2. Synthesis of $Fe_3O_4@SiO_2$

The laminated of SiO_2 from sodium silicate obtained from volcanic ash was conducted by a procedure as follow: 2 g of the prepared Fe_3O_4 was dispersed into 400 mL deionized water with ultrasonic at 50 °C for 30 min to form suspension. Then 40 mL of Na_2SiO_3 solution 2.5 M is added to the suspension along with magnetically stirring for about 1 h. That mixture was adjusted at pH 6 by addition of HCl 2 M in ultrasonic shaker for 3 h. After that, the mixture was washed with deionized water until neutral and then was dried at 80 °C. The mixture was cleaned again with ethanol to remove the free SiO_2 and then was immersed in HCl 1 M for 12 h to remove the unlaminated of Fe_3O_4. Finally, the pure of $Fe_3O_4@SiO_2$ formed was cleaned with deionized water and dried at 80 °C for 2 h.

2.2.3. Synthesis of $Fe_3O_4@SiO_2/CTA-Br$

The recoverable modified positive charge surfaced adsorbent noted as $Fe_3O_4@SiO_2/CTA-Br$ was prepared by mixing of 3 g $Fe_3O_4@SiO_2$ into 50 mL CTA-Br solution with various mol concentrations for 0.000; 0.125; 0.250; 0.500; and 1.00 mmol. The mixture was stirred for 17 h at room temperature. The residual CTA-Br was rinsed with deionized water to remove the left bromine ion then it was dried in the oven at 80 °C for about 2 h.

2.2.4. Characterization of modified adsorbent

The modified $Fe_3O_4@SiO_2/CTA-Br$ adsorbents containing 0.000; 0.125; 0.250; 0.500; and 1.00 mmol of CTA-Br as well as Fe_3O_4 were characterized using Scanning Electron Microscopy (SEM) JSM-6510 to observe the surface microstructure. Transmission Electron
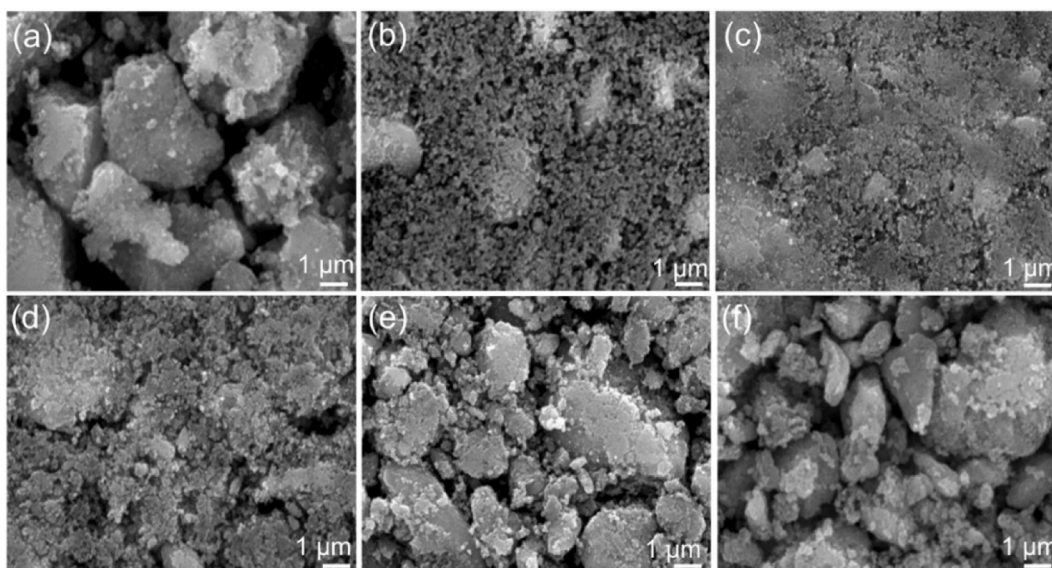
Fig. 1. Surface morphology of (a) Fe_3O_4, (b) $Fe_3O_4@SiO_2$, (c) $Fe_3O_4@SiO_2/CTA-Br$ 0.125, (d) $Fe_3O_4@SiO_2/CTA-Br$ 0.25 (e) $Fe_3O_4@SiO_2/CTA-Br$ 0.5, and (f) $Fe_3O_4@SiO_2/CTA-Br$ 1.0 through SEM represent the influence CTA-Br to enhance the surface characteristic of adsorbent.

Microscopy (TEM) JEOL is used to observe the nano-structure of modified adsorbent. Specific surface area (SSA) and the porosity were measured by the Brauner, Emmett, and Teller (BET) method using a FlowPrep060 system, via nitrogen adsorption and desorption at 77 K. The Fourier Transform Infrared (FTIR) spectra of all adsorbents were recorded on FTIR Shimadzu Prestige 21 using the KBr pellet technique in the range of 4000–300 cm^{-1} to detect the functional group changes. The X-ray Diffractometer (XRD) Rigaku Miniflex600 used to characterize the crystalline inorganic phase in the 2θ range from 20 to 80° and 0.02 step size. Unadsorbed Cr(VI) concentration was monitored using Atomic Absorption Spectrometry (AAS) PerkinElmer 3110. The turbidity of adsorbent before and after separation with magnetic field also wasevaluated by Thermo-Scientific Orion AQ4500 Turbidimeter.

2.2.5. Adsorption studies of Cr(VI)

The removal of Cr(VI) in the solution by using an adsorbent of Fe$_3$O$_4$@SiO$_2$/CTA-Br was assessed by batch technique [16] in which the effects of CTA-Br loaded and the dose of the Fe$_3$O$_4$@SiO$_2$/CTA-Br were evaluated. The stock solutions of Cr(VI) were prepared from analytical grade of K$_2$Cr$_2$O$_7$. The adsorption studies of Cr(VI) were carried out in the polyethylene tubes by batch method containing adsorbate solution and desired amount of modified adsorbent at a speed of ~60 rpm on a roller shaker. In each adsorption process, the separation of the after used adsorbent from solution was conducted by using an external magnetic field. The adsorption studies were conducted to determine the adsorption ability of Fe$_3$O$_4$@SiO$_2$/CTA-Br adsorbent affected by different CTA-Br mol concentrations, adsorbent mass, pH solution, adsorbate initial concentration, adsorption time as the main factor influencing the adsorption efficiency [15], and as well as the adsorption capacity (Supplementary 2).

The removal efficiency of Cr(VI) ions by Fe$_3$O$_4$@SiO$_2$/CTA-Br adsorbent was calculated referring to the difference among the initial (C_i) and equilibrium (C_e) concentrations of pollutants in the liquid phase after the separation. The removal efficiency of Cr(VI) pollutants and adsorption capacity of Fe$_3$O$_4$@SiO$_2$/CTA-Br were calculated by the following equations [33,34]:

$$\text{Adsorption } (\%) = \frac{C_i - C_e}{C_i} \; x \; 100\% \tag{1}$$

$$Q_e = \frac{v \, (C_i - C_e)}{W} \tag{2}$$

Where C_i and C_e are the initial and equilibrium of metal ions concentration. Q_e are equilibrium adsorption capacity. W is the adsorbent weight (mg) and v is the volume of metal ion solution (L).

3. Results and discussion

3.1. Characterization results

3.1.1. Morphological feature by SEM

To assess the character of adsorbent surface, the morphological feature of Fe$_3$O$_4$, Fe$_3$O$_4$@SiO$_2$, Fe$_3$O$_4$@SiO$_2$/CTA-Br 0.125, Fe$_3$O$_4$@SiO$_2$/CTA-Br 0.25, Fe$_3$O$_4$@SiO$_2$/CTA-Br, and Fe$_3$O$_4$@SiO$_2$/CTA-Br 1.0 were taken out by SEM instrument, and their images were shown in Fig. 1. It can be seen that the pristine Fe$_3$O$_4$ (Fig. 1a) is formed as big particles. Whereas, for Fe$_3$O$_4$@SiO$_2$ (Fig. 1b), the big particle appeared to be covered by smaller grains that must be SiO$_2$. The laminating on the surface of coverage grain is observed in
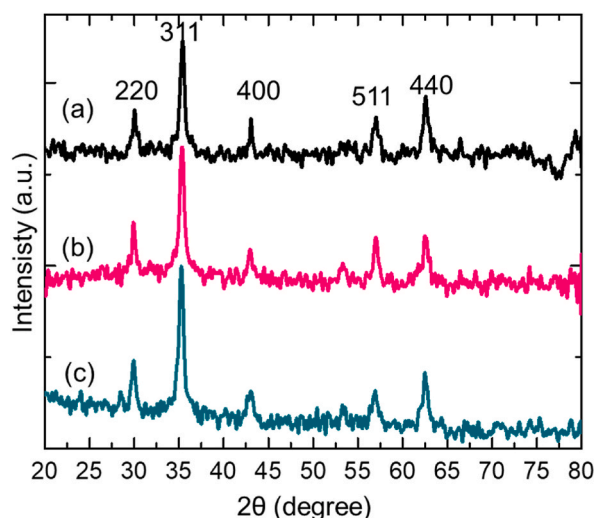
Fig. 3. The XRD pattern of (a) Fe$_3$O$_4$, (b) Fe$_3$O$_4$@SiO$_2$, and (c) Fe$_3$O$_4$@SiO$_2$/CTA-Br 0.25 mmol to confirm the present of inorganic Fe$_3$O$_4$ as the core of adsorbent.

Table 1
Surface character of adsorbent material.

Adsorbent	Surface area (m^2g^{-1})	Pore size (nm)	Total pore volume (cm^3g^{-1})
Fe_3O_4	60.1	43	0.3
$Fe_3O_4@SiO_2$	105.3	24.7	0.6
Fe3O4@SiO2/CTA-Br 0.125 mmol	122.2	17.8	0.7
$Fe_3O_4@SiO_2$/CTA-Br 0.25 mmol	147.7	13.6	0.8
$Fe_3O_4@SiO_2$/CTA-Br 0.50 mmol	126.2	23.5	0.5
$Fe_3O_4@SiO_2$/CTA-Br 1.00 mmol	113.2	35.8	0.4
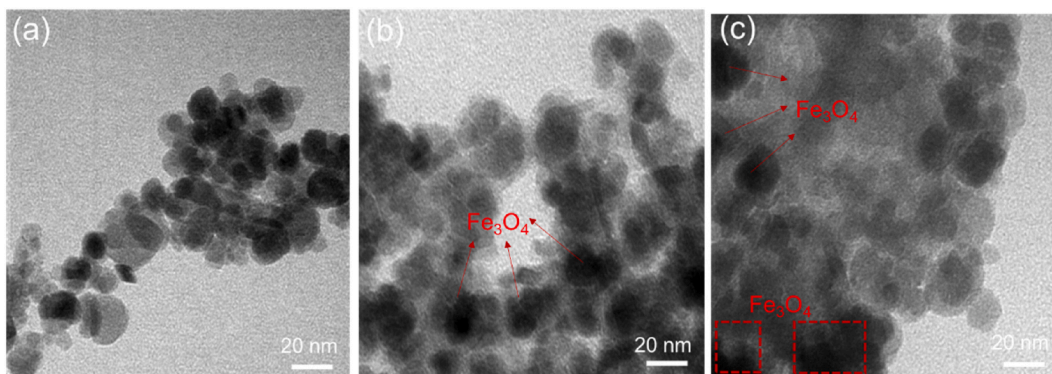
Fig. 2. The TEM images of (a) Fe_3O_4, (b) $Fe_3O_4@SiO_2$, (c) $Fe_3O_4@SiO_2$/CTA-Br 0.25 mmol.

the adsorbent of $Fe_3O_4@SiO_2$/CTA-Br (Figs. 1c and d) due to the presence of CTA-Br. It is appeared the thicker layers laminating the grain when the amount of CTA-Br in the $Fe_3O_4@SiO_2$/CTA-Br is elevated into 0.25 mmol. The thick coverage would have dealt with favorable interaction between SiO_2 and CTA-Br [28]. However, further increasing the CTA-Br loaded (0.5 and 1.0 mmol) is found to reduce the coverage area (Figs. 3e and f). This phenomenon is caused by the peeling out of the coating in the more amount of CTA-Br. The peeling out may be created by stronger bonding among the CTA-Br molecules than between CTA-Br molecules with SiO_2 layer. This result inferred that the surface morphology was dependent on the CTA-Br loading ratio, which played a significant role in the adsorbent structure to control its adsorption capacity and effectivity [35].

This result of SEM is also parallel with the surface area assessment shown in Table 1. By coverage of SiO_2 it can increase the surface area besides the bare characteristic of Fe_3O_4 that also has large specific surface area for adsorption [36]. By addition of CTA-Br the surface area also gets higher and obtain the maximum in $Fe_3O_4@SiO_2$/CTA-Br 0.25 mmol. Additionally, the pore size of $Fe_3O_4@$-SiO_2/CTA-Br 0.25 mmol also gives the smallest number but the highest total pore volume among others. Thus, the sample is chosen for the optimum adsorbent properties in further adsorption testing.

3.1.2. Nano-structural evaluation by TEM

To ascertain of surface topography with more differentiated in nano-scale, the TEM images of Fe_3O_4, $Fe_3O_4@SiO_2$, and $Fe_3O_4@SiO_2$/CTA-Br 0.25 mmol are provided in Fig. 2. The synthesized Fe_3O_4 is shown as dark spot representing the heavy molecule of iron oxide (Fig. 2a) [37]. Meanwhile, by laminating the core of Fe_3O_4 with SiO_2 it gives in the outer layer suggesting that the amorphous SiO_2 has contributed to make a new sphere on the top of Fe_3O_4 core (Fig. 2b). The position of Fe_3O_4 as the core-shell inside of the structure is also shown in the $Fe_3O_4@SiO_2$/CTA-Br 0.25 mmol image where the larger-grey with more grey colored sphere is observed that should be CTA-Br covering the dark spot of Fe_3O_4. The dark spots of Fe_3O_4 in addition to give magnetic recoverability, it also has potential to provide adsorption active surface that can enhance the adsorption capacity [38]. For supporting this structure framework, the schematic illustration of Fe_3O_4, $Fe_3O_4@SiO_2$, and $Fe_3O_4@SiO_2$/CTA-Br 0.25 mmol is provided in Scheme 1. This finding may lead to evaluate more about the chemical constituent that found in adsorbent structure.

3.1.3. Compositional of crystalline phase through XRD

The characterization of the crystalline phase obtained from XRD patterns of the prepared adsorbents were displayed in Fig. 3. In the

Table 2
The average particle size of Fe_3O_4 in the silica adsorbent materials.

Material	D (nm)
Fe_3O_4	8.04
$Fe_3O_4@SiO_2$	8.26
$Fe_3O_4@SiO_2$/CTA-Br 0.25 mmol	9.17

figure, several peaks appear at 30.01°, 35.43°, 43.03°, 57.01° and 62.57° of the two theta. The XRD data are in good agreement with the standard XRD pattern of magnetite (Fe_3O_4) with the Miller Index of 220, 311, 400, 511, and 440, respectively, as presented in JCPDS card No. 19-0629 [39]. It is clearly confirmed that Fe_3O_4 crystal has been formed. The peaks appearing in the XRD patterns of Fe_3O_4@SiO_2, and that of Fe_3O_4@SiO_2/CTA-Br are same as observed in the XRD data of Fe_3O_4, and no new peaks are detected. It is implied that the coating of amorphous SiO_2 as well as of SiO_2/CTA-Br layers on Fe_3O_4 surface did not change the structure of Fe_3O_4 crystal. Furthermore, the coating SiO_2 leads to a decrease in the intensities of the XRD pattern of Fe_3O_4, and the intensities are further decreased when the SiO_2/CTA-Br was coated on Fe_3O_4 surface [32]. The trend can also be confirmed from crystallinity index calculated in percentage assigned the ratio of area for all crystalline peaks to the area for both crystalline and amorphous phase. The synthesized pristine Fe_3O_4 by co-precipitation method resulted crystalline index 44.37 %. The crystallinity index of Fe_3O_4@SiO_2 is found as 61.07 %, where the increment of the index might be caused by additional composition of SiO_2. For Fe_3O_4@SiO_2/CTA-Br the index is about 57.09 % and the slight index decrement would be come due to amorphous CTA-Br. From the comprehensive XRD result, it is suggested that the Fe_3O_4 crystal was successfully used as a magnetic center of the Fe_3O_4@SiO_2/CTA-Br adsorbent. This finding is also reported by other authors [30,40].

$$D = \frac{k\lambda}{\beta \cos \theta}$$ [3]

Additionally, from XRD data the average particle size of the pristine and Fe_3O_4 and on the modified adsorbents have also been determined by, following *Scherrer* equation [Eq. (3)]. From the equation, *D* refers to the average particle size (nm), *k* is the crystallite shape factor (0.9), λ represents wavelength of X-ray (nm), β is the FWHM from XRD pattern (rad), and θ is the degree from a half of 2θ in the x axis of XRD pattern.

Table 2 displayed the average particles size of crystalline phase of Fe_3O_4 based on the XRD peaks in Fe_3O_4, Fe_3O_4@SiO_2, and Fe_3O_4@SiO_2/CTA-Br. As seen in the table, coating SiO_2 can enlarge the particle size of Fe_3O_4, and the attachment of CTA-Br on Fe_3O_4@SiO_2 has further increased the particle size of Fe_3O_4. It is implied that Fe_3O_4 acts as a core, while SiO_2 and SiO_2/CTA-Br coat the core as a shell. Similar finding has also been reported previously [41].

3.2. Compositional and interaction through FTIR

In order to know the better interactions between Fe_3O_4 with SiO_2 and between SiO_2 with CTA-Br, the FTIR spectra of Fe_3O_4, Fe_3O_4@SiO_2, CTA-Br, and Fe_3O_4@SiO_2/CTA-Br are recorded and depicted in Fig. 4. For pure Fe_3O_4, several peaks observed are 578 cm^{-1} corresponding to the characteristic absorption peak of the Fe–O bond, and 1635 cm^{-1} and 3441 cm^{-1} assigning to –OH group of Fe–OH, respectively [41]. Meanwhile in the spectra of the pure SiO_2 shows some peaks at 956 cm^{-1}, 1095 cm^{-1}, 578 cm^{-1}, and 470 cm^{-1} are attributed to the symmetric and asymmetric vibrations of Si–O–Si bond, respectively [42]. In addition, broad peak appearing at 3410 cm^{-1} is also seen in Fig. 4b, which corresponds to the bending vibration of O–H bond of Si–OH. On the other hand, the spectra of the pure CTA-Br (Fig. 4d) exhibits a broad absorption peak at 3094 cm^{-1}, that represents the bending vibration of hydrogen in N–H and peak at around 987 cm^{-1} assigned to C–N^+. Furthermore, the absorption peaks at 2916 and 2848 cm^{-1} shown in Fig. 4d may correspond to the asymmetric and symmetric stretching vibration of CH_2 respectively [4]. The peaks seen at 1481 cm^{-1} is attributed to nitrogen in N–H from CTA-Br. The peaks at 965 and 912 cm^{-1} assigned to the asymmetric and symmetric stretching vibration of C–N^+ bond, respectively. Besides, other peaks for all spectra that were identified at around 1640 cm^{-1} and 2361 cm^{-1} assigned to the present of H_2O and CO_2 gas during measurement [25].

For the composites material, The FTIR mode of Fe_3O_4@SiO_2 (Fig. 4c) illustrates that the peak of Fe–O bond shifting to 586 from 578 cm^{-1} and that of Si–O–Si are shifting to 1087 cm^{-1} and 455 cm^{-1} from 1095 cm^{-1} and 470 cm^{-1} respectively. The shift from 965 into 964 cm^{-1} on the bending vibration of Si–O–Si is also observed. Furthermore, the intensity of the Si–OH adsorption peak at 965 cm^{-1} significantly decreased after the formation of Fe_3O_4@SiO_2. These data imply that the interfaces of Fe_3O_4 and SiO_2 in the Fe_3O_4@SiO_2 have Fe–O–Si covalent bonding because of OH condensation [43]. The covalent bonding suggests that Fe_3O_4@SiO_2 is formed as a composite. This data agrees with their XRD patterns with respect to the decreasing intensities. In the FTIR pattern of Fe_3O_4@SiO_2/CTA-Br (Fig. 4e), some absorptions are found to shift from 3410 cm^{-1} into 3425 cm^{-1}, from 2916 into 2924 cm^{-1}, and from 1481 into 1381 cm^{-1}. Such shifts may be affected by the interaction between –HN^+ - of CTA-Br with O–H belonged to Si–OH from silica. Therefore, the positive charge is expected from –NH^+ group to form on the adsorbent surface.

3.3. Adsorption study of Cr(VI)

3.3.1. Influence on the amount of the CTA-Br loaded in the adsorbent

The results of the adsorption of Cr(VI) anionic by the adsorbents of Fe_3O_4@SiO_2 (shown with the CTA-Br concentration 0.000 mmol) and Fe_3O_4@SiO_2/CTA-Br with various CTA-Br loading are exhibited in Fig. 5.

In the Fig. 5, Fe_3O_4@SiO_2 adsorbent shows very low ability in the Cr(VI) anionic adsorption, and considerable enhancement of the adsorption is exhibited for Fe_3O_4@SiO_2/CTA-Br. The low adsorption of the anionic by Fe_3O_4@SiO_2 may be due to the physical entrapment because the adsorbent surface has negative charges, provided by silica surface [28,36] that must refuse the Cr(VI) anion. The higher adsorption of the anionic on the Fe_3O_4@SiO_2/CTA-Br is generated from positive surface provided by –NH^+ group in CTA-Br. Increasing CTA-Br fraction resulted in the higher adsorption, but the CTA-Br fraction larger than 0.25 leads to a dismiss the adsorption.

The low adsorption found in Fe_3O_4@SiO_2/CTA-Br with low CTA-Br loading may be caused by the fact that the surface of adsorbent
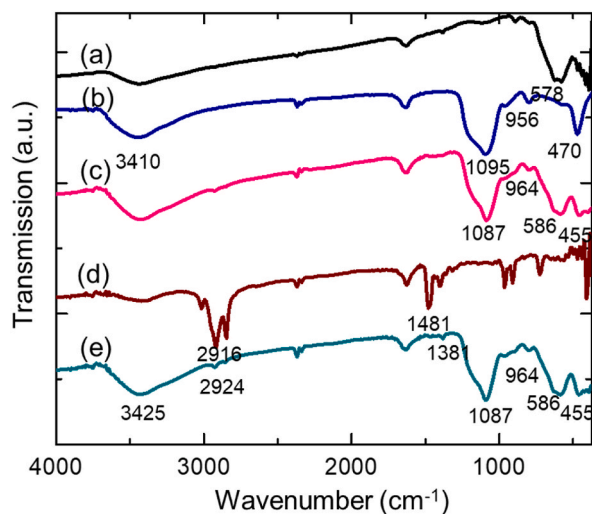
Fig. 4. The FTIR spectra of (a) Fe_3O_4, (b) SiO_2, (c) $Fe_3O_4@SiO_2$, (d) CTA-Br, and (e) Fe3O4@SiO2/CTA- Br 0.25 mmol for confirming the composition and interaction between the material constituents on the adsorbent.
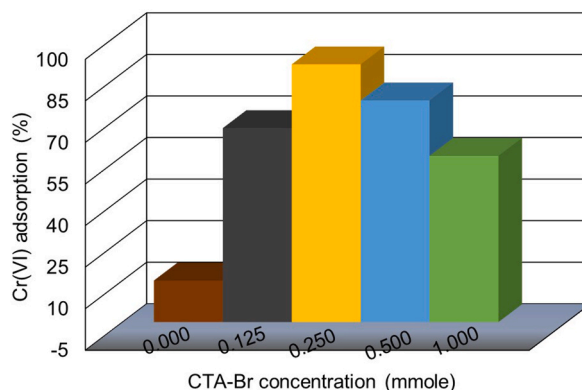
Fig. 5. Adsorbent performance of $Fe_3O_4@SiO_2/CTA$-Br with different CTA-Br concentrations to obtain the optimum ratio.
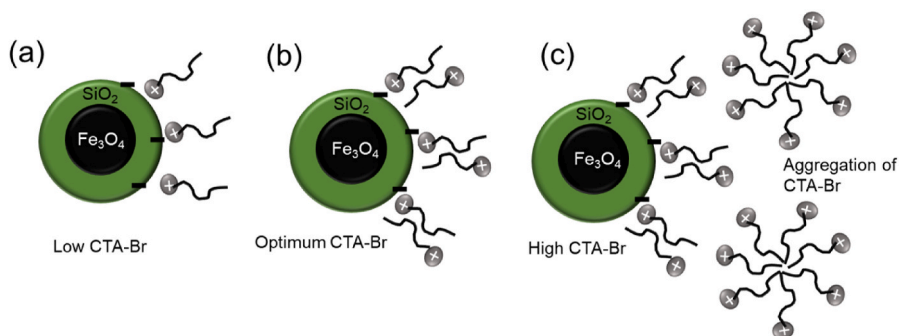
Fig. 6. Schematic illustration on the effect of CTA-Br loaded to the $Fe_3O_4@SiO_2/CTA$-Br adsorbent in the (a) low concentration without bilayer, (b) optimum concentration shown positive charge bilayer, and the (c) excess concentration with aggregation.

remained in hydrophobic as illustrated by Fig. 6a. The positive charge of CTA-Br may be still dominated to attach the O from Si–O of silica. Consequently, the outer layer of the core-cell of $Fe_3O_4@SiO_2$ were consists of the alkyl tail of CTA-Br making non-polar properties as well as the hydrophobic condition. This hydrophobic position prevented the adsorption of anionic Cr(VI) through electrostatic interaction.

The increase of the CTA-Br loading from 0.25 mmol to 0.5 mmol, has continued to improve the adsorption but with higher loading than 0.5 mmol leads to adsorption decrement. When the amount of CTA-Br is equal to or higher than its CMC (critical micelle concentration), a bilayer of the carbon chain of CTA-Br could be formed that gave a positive charge on the adsorbent surface, as seen in the illustration in Fig. 6b [44]. The positive surface induced the most effective adsorption of the anionic Cr(VI) that is 93 %. A decline in the adsorption shown by very large CTA-Br content, may be affected by formation of CTA-Br aggregation (Fig. 6c), followed by the release of the CTA-Br bilayer as reduces the adsorption sites, resulting in the lower adsorption effectiveness as illustrated in Fig. 5. From the series data, it is clearly assigned that 0.25 mmol is the optimum CTA-Br concentration.

3.3.2. Influence of the adsorbent dose

To find the optimum adsorbent dose, an assessment was carried out. With the adsorbent dose variation and the results were displayed in Fig. 7a. It can be seen in Fig. 7a that the adsorption elevation is notable as the enlargement of the amount of adsorbent mass up to 0.25 g gives maximum removal of Cr(VI) in 95.5 %. The larger of the adsorbent mass, hence the more positive charges were available [45]. But the excessive adsorbent amount leads to the saturated adsorption process assigned from the slight decrement of Cr (VI) removal due to the agglomeration of the adsorbent itself which avoid the adsorption sites to entrap the adsorbate.

3.3.3. Influence of the solution pH

The adsorption effectiveness, generally is considerably affected by pH of the solution, since the pH controls the charges of both adsorbent and adsorbate (Cr(VI)) in the solution. The result from Fig. 7b depicts that at the very low pH, the low adsorption is observed, and the adsorption is gradually increased when the solution pH was enhanced into 3. In the solution with higher pH than 3, the contrary effect obviously appears. These findings are in good agreement with the previous achievement [47,48]. It is reported that the pH of the zero point charge of CTA-Br is found to be 4 [36], implying that at pH lower than 4, the charge of CTA-Br is positive, and the negative charge exists at pH higher than 4. Meanwhile, in the solution at pH lower than 3, Cr(VI) are formed as $HCrO_4^-$ and low fraction of CrO_4^{2-} allowing them to have weak affinity with the adsorbent surface. With the increase of up to 3, the species of CrO_4^{2-} and $Cr_2O_7^{2-}$ are formed serving the conductive adsorption through electrostatic interaction with protonated nitrogen from CTA-Br [1,6]. At pH higher than 4, the gradual adsorption decrease is observable, where the negative charges of both adsorbent surface and the adsorbate were available repulsing them to mutually interact. Additionally, it may also be caused by the more competition between Cr (VI) anionic with the more OH^- present. Thereby, the removal of anionic Cr(VI) was inhibited [46]. It is evident that the optimum pH for Cr(VI) adsorption is 3.

3.3.4. Influence of Cr(VI) initial concentration

The study in the influence of Cr(VI) initial concentration was used for determining the adsorption capacity. From the result in Fig. 8a the sharp line of increment occurred when the initial concentration of adsorbate is around 2.5–25 mgL^{-1}. Whereas, a slight increment led to the steady state occurring in the range concentration of 25–100 mgL^{-1}. This phenomenon is caused that in range concentration 2.5–25 mgL^{-1}, the amount of anionic Cr(VI) is still possible to attach in the active surface of adsorbent. While, in the concentration over 25 mgL^{-1}, adsorbent was in saturated condition, thus it could not give further increment of adsorption.

3.3.5. Influence of adsorption time

The assessment for the adsorption process was also conducted in various contact times as illustrated in Fig. 8b. As the time elapses, Cr(VI) adsorption rises until 60 min. Fast adsorption in the early stages is responsible to the larger concentration gradient which can lead to higher driving forces and higher availability of vacant active surface in the adsorbent [25]. At a contact time of more than 60 min, the adsorption percentage gets stagnant due to adsorbate amount that might already be entrapped in the adsorbent. This disclosure of influence in initial Cr(VI) concentration and adsorption time are used to understand the isotherm model.
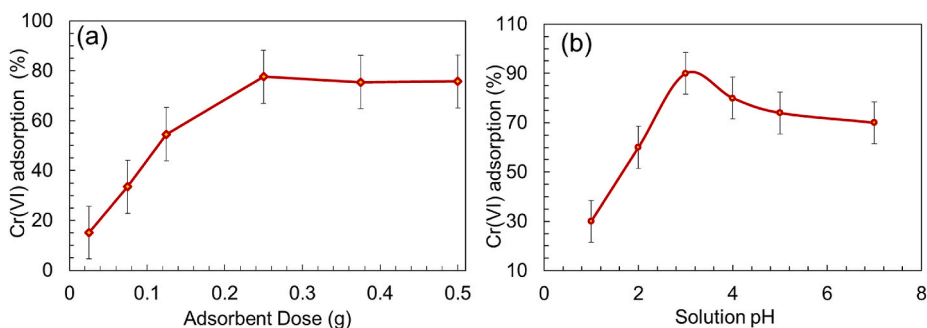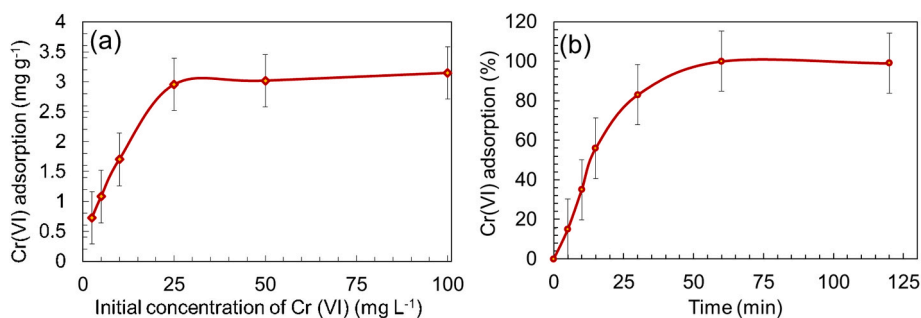

Fig. 7. Effect of (a) Fe$_3$O$_4$@SiO$_2$/CTA-Br amount and (b) pH condition on Cr(VI) adsorption. Cr(VI) concentration = 25 mg L^{-1} , solution volume = 20 mL.

Fig. 8. Effect of (a) initial concentration of Cr (VI) and (b) contact time on the adsorption performance. Cr(VI) concentration = 25 mg L^{-1}, solution volume = 20 mL.

3.3.6. Adsorption thermodynamics

3.3.6.1. Influence of temperature. Since adsorption is a dynamic process, the change in the temperature can affect the adsorption performance, this study provide the influence of temperature on Cr(VI) adsorption using Fe$_3$O$_4$@SiO$_2$/CTA-Br 0.25 mmol, shown in Fig. 9. The assessment was conducted at variation temperature between 20 and 70 °C. According to result in Fig. 9, as the adsorption temperature elapses the adsorption efficiency is likely getting increase. That tendency works until reaches the optimum at 35 °C. After reaching the optimum temperature, in the higher temperature than 35 °C the adsorption of Cr (VI) begins to decrease due to possibility on the desorption process of adsorbate. This trend assumes that the adsorption process using Fe$_3$O$_4$@SiO$_2$/CTA-Br 0.25 mmol walks in an exothermic condition [36].

3.3.6.2. Isotherm model. The adsorption isotherm explains the migration and retention of adsorbate from aqueous environment to the solid phase of adsorbent at optimum pH and adsorbent mass that obtained. This assessment was done by observing the adsorption tendency for various initial concentrations of adsorbate in which the interaction between adsorbate and adsorbent could be understood by two conventional model of isotherm that are Langmuir and Freudlich [47]. From the result provided in Fig. 10 and Table 3, the R^2 value for Langmuir and Freudlich are 0.9976 and 0.9144, respectively. Thus, the adsorption mechanism of Fe$_3$O$_4$@SiO$_2$/CTA-Br in a bid Langmuir isotherm. It implied that the surface of adsorbent is homogenous and the adsorption forms monolayer in which each active surface is uniformly distributed to attract one adsorbate molecule and could not continually adsorb [48,49]. From the calculation of Langmuir isotherm, the maximum adsorption capacity (Q_{max}) for Fe$_3$O$_4$@SiO$_2$/CTA-Br is 3.38 mg g^{-1} and adsorption energy (E_{ads}) is 22.56 kJmol^{-1}. The number of adsorption energy was higher than 20.92 kJ mol^{-1} as the minimum requirement for chemisorption. Meanwhile from that calculation based on a linear fit curve, also obtained, K_L and K_F as Langmuir and Freudlich constant respectively and n is heterogeneity factor. In addition, the heterogeneity factor from Freudlich equation which n > 1 indicates that van Der Waals force and electrostatic interaction are exist in the Fe$_3$O$_4$@SiO$_2$/CTA-Br adsorbent [41,48]. This finding leads to infer that the adsorption process of Cr(VI) anionic has occurred through chemisorption. The mechanism of chemisorption starts from physisorption assigned from the approaching of Cr(VI) anionic to the adsorbent surface through Van Der Waals force [35,41]. Then, the anion promoted the chemical bonding as electrostatic interaction with protonated amine from CTA-Br in Fe$_3$O$_4$@SiO$_2$/CTA-Br [50]. Therefore, the whole mechanism of chemisorption also involves physisorption in the beginning process of adsorbent contact surface, which corroborates that the surface nature of adsorbent is highly dependent to the Cr(VI) adsorption.

3.3.7. Adsorption kinetics

The study of adsorption kinetics in Fe$_3$O$_4$@SiO$_2$/CTA-Br 0.25 mmol were investigated using Lagergren pseudo-first-order equation and pseudo-second order equation as the general representative model for heavy metal adsorption such as in Cr(VI) using the solid
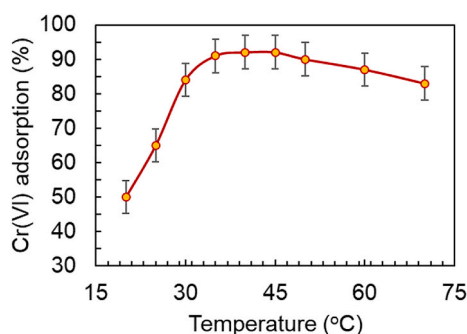
Fig. 9. The influence of temperature on Cr(VI) adsorption using Fe$_3$O$_4$@SiO$_2$/CTA-Br 0.25 mmol.
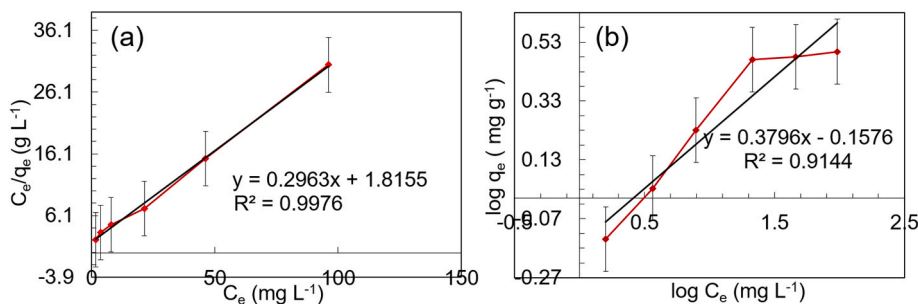
Fig. 10. Adsorption isotherm of $Fe_3O_4@SiO_2/CTA-Br$ 0.25 mmol plotted in (a) Langmuir and (b) Freundlich.

Table 3
Adsorption parameters of $Fe_3O_4@SiO_2/CTA-Br$ adsorbent provided by Langmuir and Freundlich isotherm.

Isotherm	Langmuir model				Freundlich model		
	Q_{max} (mg g^{-1})	K_L (L mg^{-1})	E_{ads} (kJ mol^{-1})	R^2	n	K_F (mg g^{-1})	R^2
	3.38	8.49	22.56	0.998	2.63	0.70	0.914

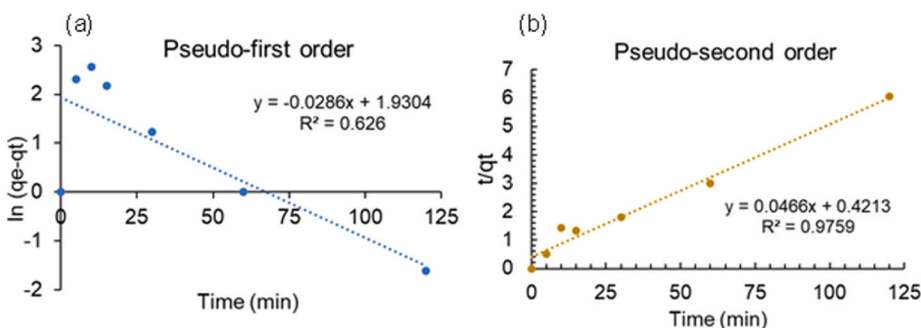**Fig. 11.** Kinetic models in (a) pseudo-first order and (b) pseudo-second order for $Fe_3O_4@SiO_2/CTA-Br$ 0.25 mmol in removing Cr(VI).

Table 4
Kinetics parameter of $Fe_3O_4@SiO_2/CTA-Br$ 0.25 mmol in removing Cr(VI).

Kinetics	Pseudo-first order			Pseudo-second order		
	q_e (mg g^{-1})	ki (min^{-1})	R^2	q_e (mg g^{-1})	k_2 (g mg^{-1} min^{-1})	R^2
		0.028	0.626	21.46	0.005	0.976

phase adsorbent material [46]. The pseudo-first order equation is used to explain the fast adsorption of adsorbate from solution and the process which predominantly controlled by diffusion [4]. Here, the equation from pseudo-first order [Eq. (4)].

$$\ln(q_e - q_t) = \ln q_e - (k_1 \times t) \tag{4}$$

Whereas, the pseudo-second order [Eq. (5)] is expressing the kinetic model based on chemisorption [26].

$$\frac{t}{q_t} = \frac{1}{k_2 q_e^2} + \left(\frac{1}{q_e}\right) \times t \tag{5}$$

Where k_1 is the pseudo-first order rate constants, k_2 is the pseudo-second ordered, q_t is amount of Cr(VI) in certain time and q_e denotes the equilibrium amount of Cr(VI) adsorption. Based on the data obtained from assessment of influence time in adsorption process the kinetic model can be plotted in Fig. 11 and the parameter is provided in Table 4.

According to the calculation, the pseudo-second order is well-fitted to the adsorption of Cr(VI) by $Fe_3O_4@SiO_2/CTA-Br$ shown by R^2 that close to 1. It means that the rate-controlling step is controlled by electrostatic interaction between protonated ammonium from CTA-Br with anionic of Cr(VI) [46]. Besides, this model also supports the chemisorption mechanism.

To compare this study with other report in removal of Cr(VI) through adsorption the data in Table 5 was provided. It can be concluded that the adsorption of Cr(VI) using inorganic and organic adsorbent are mostly fitted in Langmuir isotherm and pseudo-second order in kinetics model including this study. The different number of adsorption capacity might be caused by different adsorbent dosage, reaction time, and the initial concentration of adsorbent. However, both of them support that the adsorption of

Table 5

Comparison adsorbent performance in reducing Cr(VI) contaminant through various method and material.

No	Adsorbent	Method	Adsorption capacity/Q_C (mg/g)	Kinetics model	Isotherm	Ref
1.	Fly ash	Multistep treatment	41.3	–	Langmuir Freudlich	[51]
2.	Mango kernel activated carbon	Carbonization and H_3PO_4 activation	7.1	Pseudo-second order	Langmuir	[52]
3.	Magnetic corn straw biochar	Co-precipitation	138.8	Pseudo-second order	Langmuir	[2]
4.	Magnetic wood biochar	Co-precipitation	78.7	Pseudo-second order	Langmuir	[53]
5.	Kaolin-CTA-Br	Co-precipitation	22.7	Pseudo-second order	Langmuir	[46]
6.	Carbonized coal-CTA-Br	Oxidation process	78.7	Pseudo-second order	Langmuir	[43]
7.	Phytic acid	Ultrasonic	367.9	Pseudo-second order	Langmuir	[4]
8.	Mg–Zn ferrite	Sol-gel	30.5	–	Langmuir	[15]
9.	Thiolated chitosan	Microwave irradiation	340.1	Pseudo-second order	Freudlich	[1]
10.	$MnFe_2O_4@SiO_2.CTA-Br$	Hydrothermal	24.0	Pseudo-second order	Freudlich	[37]
11.	Titania tubes	Alkaline hydrothermal	43.0	Pseudo-second order	Langmuir	[13]
12.	Nutshell-activated carbon	Chemical activation	46.2	Pseudo-second order	Langmuir	[34]
13.	$Fe_3O_4@SiO_2/CTA-Br$	Co-precipitation	3.38	Pseudo-second order	Langmuir	This study

anionic Cr(VI) is controlled by the interaction of the adsorbate and active site of adsorbent, and tend to be a chemisorption process.

3.3.8. Effect of adsorption and separability process

The phenomena of the adsorption process were also determined from the characteristic in FTIR spectra of $Fe_3O_4@SiO_2/CTA-Br$ adsorbent in comparison before and after adsorption. Fig. 12a showed that the sharp band was found at around 1381 cm^{-1} corresponding to the presence of ammonium in CTA-Br before the adsorption process. However, that band getting weak in the condition of characterization adsorbent after use, indicated that the protonated ammonium was getting bound strongly with anionic Cr(VI) [54]. Nevertheless, for the overall absorption band FTIR spectra does not appear significant change respected to the different functional group. It means that, there are also no alteration of the adsorbent structure which still supports the chemical stability of the adsorbent. The other interesting finding of adsorption $Fe_3O_4@SiO_2/CTA-Br$ is the performance in self-separation triggered by external magnetization as illustrated in Figs. 12b and c. The dispersion of adsorbent and Cr(VI) in aqueous condition is found in Fig. 12b contacted after the adsorption process. Before 1 min it was anticipated to perfectly separate between powdered adsorbent with adsorbate in aqueous media using a magnet rod (Fig. 12c). This performance of adsorbent would make an efficient and effective separation process to make the adsorption process is practical.
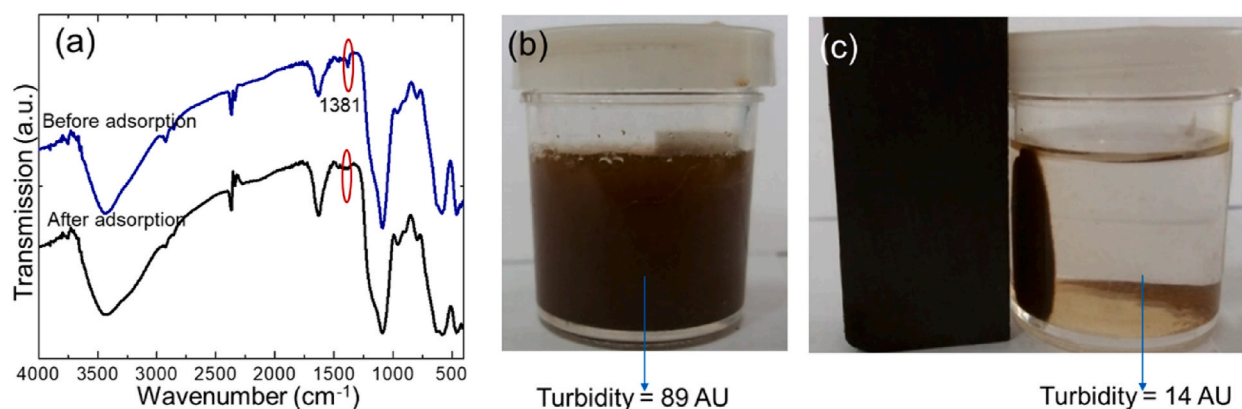
Fig. 12. (a) The effect of the adsorption process of $Fe_3O_4@SiO_2/CTA-Br$ observed from FTIR-spectra, (b) separation process after adsorption with the magnetic rod shows the initial condition and (c) after contact with magnetic rod with the change of turbidity value from 89 AU to 14 AU.

4. Conclusion

In this recount, the recoverable adsorbent from Merapi volcanic ash of Fe_3O_4@SiO_2/CTA-Br was prepared by precipitated of Fe_3O_4 and modified with CTA-Br to induce the adsorption effectivity of anionic Cr(VI). In an effort to improve the removal efficiency of this contaminant, the ratio of CTA-Br was controlled during laminated process. The Fe_3O_4@SiO_2/CTA-Br 0.25 mmol is gained as the optimum condition in which the bilayer CTA-Br formed effectively as it provides the negative active surface of adsorbent. Then, the adsorption of anionic Cr(VI) using Fe_3O_4@SiO_2/CTA-Br was evaluated for the adsorbent mass, pH condition and contact time which resulted in 0.25 g adsorbent is the appropriate amount to adsorb Cr(VI) in pH 3 for 60 min. The adsorption of Cr(VI) using Fe_3O_4@SiO_2/CTA-Br 0.25 mmol follows Langmuir model and pseudo-second-order with adsorption capacity (Q_{max}) is 3.38 mg g^{-1} adsorption energy is 22.56 kJ mol^{-1}, and kinetics constant at 0.005 g mg^{-1} min^{-1} evidencing the chemisorption from electrostatic interaction of protonated ammonium in CTA-Br with the anionic Cr(VI). The existence of Fe_3O_4 as a cored-cell adsorbent also pronounced the feasible separation performance with magnetization properties.

CRediT authorship contribution statement

Early Zahwa Alharissa: Formal analysis, Validation, Visualization, Writing – review & editing. **Yuanita Efhiliana:** Conceptualization, Formal analysis, Investigation, Methodology. **R. Roto:** Project administration, Supervision, Validation. **M. Mudasir:** Project administration, Supervision, Validation. **Endang Tri Wahyuni:** Data curation, Formal analysis, Methodology, Supervision, Writing – original draft, Writing – review & editing.

Declaration of competing interest

The authors declare that they have no known competing financial interests or personal relationships that could have appeared to influence the work reported in this paper.

Acknowledgements

Appendix A. Supplementary data

Supplementary data to this article can be found online at https://doi.org/10.1016/j.heliyon.2023.e23273.

References

[1] A. Shekhawat, S. Kahu, D. Saravanan, S. Pandey, R. Jugade, Rational modification of chitosan biopolymer for remediation of Cr(VI) from water, J. Hazardous Mater. Adv. 7 (2022), 100123, https://doi.org/10.1016/j.hazadv.2022.100123.

[2] T.T.H. Chu, M.V. Nguyen, Improved Cr (VI) adsorption performance in wastewater and groundwater by synthesized magnetic adsorbent derived from Fe_3O_4 loaded corn straw biochar, Environ. Res. 216 (2023), https://doi.org/10.1016/j.envres.2022.114764.

[3] M. Banerjee, R.K. Basu, S.K. Das, Cr(VI) adsorption by a green adsorbent walnut shell: adsorption studies, regeneration studies, scale-up design and economic feasibility, Process Saf. Environ. Protect. 116 (2018) 693–702, https://doi.org/10.1016/j.psep.2018.03.037.

[4] K. Bouaouina, A. Barras, N. Bezzi, M.A. Amin, S. Szunerits, R. Boukherroub, Adsorption reduction of Cr(VI) onto unmodified and phytic acid-modified carob waste: kinetic and isotherm modeling, Chemosphere 297 (2022), https://doi.org/10.1016/j.chemosphere.2022.134188.

[5] S. Sobhanardakani, A. Jafari, R. Zandipak, A. Meidanchi, Removal of heavy metal (Hg(II) and Cr(VI)) ions from aqueous solutions using Fe_2O_3@SiO_2 thin films as a novel adsorbent, Process Saf. Environ. Protect. 120 (2018) 348–357, https://doi.org/10.1016/j.psep.2018.10.002.

[6] K. Liu, D. Zhao, Z. Hu, Y. Xiao, C. He, F. Jiang, N. Zhao, C. Zhao, W. Zhang, R. Qiu, The adsorption and reduction of anionic Cr(VI) in groundwater by novel iron carbide loaded on N-doped carbon nanotubes: effects of Fe-confinement, Chem. Eng. J. 452 (2023), https://doi.org/10.1016/j.cej.2022.139357.

[7] A. Alemu, B. Lemma, N. Gabbiye, M. Tadele Alula, M. Teferi Desta, Removal of chromium (VI) from aqueous solution using vesicular basalt: a potential low cost wastewater treatment system, Heliyon 4 (2018) 682, https://doi.org/10.1016/j.heliyon.2018.

[8] J.S. Castañeda-Figueredo, A.I. Torralba-Dotor, C.C. Pérez-Rodríguez, A.M. Moreno-Bedoya, C.S. Mosquera-Vivas, Removal of lead and chromium from solution by organic peels: effect of particle size and bio-adsorbent, Heliyon 8 (2022), https://doi.org/10.1016/j.heliyon.2022.e10275.

[9] X. Li, J. Liu, J. Feng, T. Wei, Z. Zhou, J. Ma, Y. Ren, Y. Shen, High-ratio {100} plane-exposed ZnO nanosheets with dual-active centers for simultaneous photocatalytic Cr(VI) reduction and Cr(III) adsorption from water, J. Hazard Mater. 445 (2023), https://doi.org/10.1016/j.jhazmat.2022.130400.

[10] E.T. Wahyuni, N.P. Diantariani, I. Kartini, A. Kuncaka, Enhancement of the photostability and visible photoactivity of ZnO photocatalyst used for reduction of Cr (VI) ions, Results in Eng. 13 (2022), https://doi.org/10.1016/j.rineng.2022.100351.

[11] S.Y. Pi, Y. Wang, C. Pu, X. Mao, G.L. Liu, H.M. Wu, H. Liu, Cr(VI) reduction coupled with Cr(III) adsorption/precipitation for Cr(VI) removal at near neutral pHs by polyaniline nanowires-coated polypropylene filters, J. Taiwan Inst. Chem. Eng. 123 (2021) 166–174, https://doi.org/10.1016/j.jtice.2021.05.019.

[12] F. Yao, M. Jia, Q. Yang, K. Luo, F. Chen, Y. Zhong, L. He, Z. Pi, K. Hou, D. Wang, X. Li, Electrochemical Cr(VI) removal from aqueous media using titanium as anode: simultaneous indirect electrochemical reduction of Cr(VI) and in-situ precipitation of Cr(III), Chemosphere (2020) 260, https://doi.org/10.1016/j.chemosphere.2020.127537.

[13] H. Li, Y. Huang, Q. Luo, J. Liu, The simultaneous reduction and adsorption for V(V) and Cr(VI) anionic species in aqueous solution by polyethyleneimine cross-linked titanate nanotubes, Sep. Purif. Technol. 299 (2022), https://doi.org/10.1016/j.seppur.2022.121682.

[14] M. Yılmazoğlu, N. Kanmaz, J. Hızal, Highly efficient sulfonated poly (ether ether ketone) (sPEEK) adsorbent for removal of uranium (VI) from aqueous solution, Process Saf. Environ. Protect. 174 (2023) 848–855, https://doi.org/10.1016/j.psep.2023.04.054.

[15] T. Tatarchuk, M. Myslin, I. Lapchuk, A. Shyichuk, A.P. Murthy, R. Gargula, P. Kurzydło, B.F. Bogacz, A.T. Pędziwiatr, Magnesium-zinc ferrites as magnetic adsorbents for Cr(VI) and Ni(II) ions removal: cation distribution and antistructure modeling, Chemosphere 270 (2021), https://doi.org/10.1016/j.chemosphere.2020.129414.

[16] A.K. Priya, V. Yogeshwaran, S. Rajendran, T.K.A. Hoang, M. Soto-Moscoso, A.A. Ghfar, C. Bathula, Investigation of mechanism of heavy metals (Cr^{6+}, Pb^{2+} & Zn^{2+}) adsorption from aqueous medium using rice husk ash: kinetic and thermodynamic approach, Chemosphere 286 (2022), https://doi.org/10.1016/j.chemosphere.2021.131796.

[17] M.S. Hosseini Hashemi, F. Eslami, R. Karimzadeh, Organic contaminants removal from industrial wastewater by CTAB treated synthetic zeolite Y, J. Environ. Manag. 233 (2019) 785–792, https://doi.org/10.1016/j.jenvman.2018.10.003.

[18] E. Gagliano, M. Sgroi, P.P. Falciglia, C. Belviso, F. Cavalcante, A. Lettino, F.G.A. Vagliasindi, P. Roccaro, Removal of ammonium from wastewater by zeolite synthetized from volcanic ash: batch and column tests, J. Environ. Chem. Eng. 10 (2022), https://doi.org/10.1016/j.jece.2022.107539.

[19] R. Haounati, H. Ouachtak, R. El Haouti, S. Akhouairi, F. Largo, F. Akbal, A. Benlhachemi, A. Jada, A.A. Addi, Elaboration and properties of a new SDS/CTAB@ Montmorillonite organoclay composite as a superb adsorbent for the removal of malachite green from aqueous solutions, Sep. Purif. Technol. 255 (2021), https://doi.org/10.1016/j.seppur.2020.117335.

[20] C. Tsioptsias, G. Samiotis, L. Lefteri, E. Amanatidou, Cr(VI) leached from lignite fly ash—assessment of groundwater contamination risk, Water Air Soil Pollut. 231 (2020), https://doi.org/10.1007/s11270-020-04750-4.

[21] H. Zhang, B. Sun, Y. Qian, T. Yang, W. Chen, CTAB-mediated lithium disilicate branched structures as superb adsorbents to remove Mn^{2+} in water, Boletin de La Sociedad Espanola de Ceramica y Vidrio, 2022, https://doi.org/10.1016/j.bsecv.2022.07.001.

[22] A.O. Egbedina, C.G. Ugwuja, P.A. Dare, H.D. Sulaiman, B.I. Olu-Owolabi, K.O. Adebowale, CTAB-Activated carbon from peanut husks for the removal of antibiotics and antibiotic-resistant bacteria from water, Environ. Process. 10 (2023) 20, https://doi.org/10.1007/s40710-023-00636-9.

[23] P.N. Lemougna, K. tuo Wang, Q. Tang, A.N. Nzeukou, N. Billong, U.C. Melo, X. min Cui, Review on the use of volcanic ashes for engineering applications, Resour. Conserv. Recycl. 137 (2018) 177–190, https://doi.org/10.1016/j.resconrec.2018.05.031.

[24] C.G. Ramos, M.L.S. Oliveira, M.F. Pena, A.M. Cantillo, L.P.L. Ayarza, J. Korchagin, E.C. Bortoluzzi, Nanoparticles generated during volcanic rock exploitation: an overview, J. Environ. Chem. Eng. 9 (2021), https://doi.org/10.1016/j.jece.2021.106441.

[25] S. Alraddadi, Utilization of nano volcanic ash as a natural economical adsorbent for removing cadmium from wastewater, Heliyon 8 (2022), https://doi.org/10.1016/j.heliyon.2022.e12460.

[26] L. Li, Y. Xu, D. Zhong, N. Zhong, CTAB-surface-functionalized magnetic MOF@MOF composite adsorbent for Cr(VI) efficient removal from aqueous solution, Colloids Surf. A Physicochem. Eng. Asp. 586 (2020), https://doi.org/10.1016/j.colsurfa.2019.124255.

[27] H. Hajjaoui, A. Soufi, M. Khnifira, M. Abdennouri, F.Z. Mahjoubi, N. Barka, Mono and binary mixture removal of eriochrome black T and Cr(VI) from water by SiO$_2$/polyaniline composite, Mater. Chem. Phys. 296 (2023), https://doi.org/10.1016/j.matchemphys.2022.127220.

[28] K. Li, Z. Zeng, J. Xiong, L. Yan, H. Guo, S. Liu, Y. Dai, T. Chen, Fabrication of mesoporous Fe$_3$O$_4$@SiO$_2$@CTAB-SiO$_2$ magnetic microspheres with a core/shell structure and their efficient adsorption performance for the removal of trace PFOS from water, Colloids Surf. A Physicochem. Eng. Asp. 465 (2015) 113–123, https://doi.org/10.1016/j.colsurfa.2014.10.044.

[29] T. R, S. Sundararaman, Synthesis and characterization of chicken eggshell powder coated magnetic nano adsorbent by an ultrasonic bath assisted co-precipitation for Cr(VI) removal from its aqueous mixture, J. Environ. Chem. Eng. 8 (2020), https://doi.org/10.1016/j.jece.2020.103877.

[30] J.Q. Ma, S.B. Guo, X.H. Guo, H.G. Ge, Liquid-phase deposition of TiO$_2$ nanoparticles on core–shell Fe$_3$O$_4$@SiO$_2$ spheres: preparation, characterization, and photocatalytic activity, J. Nanoparticle Res. 17 (2015), https://doi.org/10.1007/s11051-015-3107-1.

[31] N. Madima, K.K. Kefeni, A.T. Kuvarega, S.B. Mishra, A.K. Mishra, Visible-light-driven Z-scheme ternary Fe$_3$O$_4$/TiO$_2$/g-C$_3$N$_4$ nanocomposite as reusable photocatalyst for efficient removal of dyes and chromium in water, Mater. Chem. Phys. 296 (2023), https://doi.org/10.1016/j.matchemphys.2022.127233.

[32] Z. Al-Qodah, R. Dweiri, M. Khader, S. Al-Sabbagh, M. Al-Shannag, S. Qasrawi, M. Al-Halawani, Processing and characterization of magnetic composites of activated carbon, fly ash, and beach sand as adsorbents for Cr(VI) removal, Case Studies in Chem. Environ. Eng. 7 (2023), https://doi.org/10.1016/j.cscee.2023.100333.

[33] T. Shahnaz, V. Sharma, S. Subbiah, S. Narayanasamy, Multivariate optimisation of Cr (VI), Co (III) and Cu (II) adsorption onto nanobentonite incorporated nanocellulose/chitosan aerogel using response surface methodology, J. Water Proc. Eng. 36 (2020), https://doi.org/10.1016/j.jwpe.2020.101283.

[34] A. Kumar, H.M. Jena, Adsorption of Cr(VI) from aqueous phase by high surface area activated carbon prepared by chemical activation with ZnCl$_2$, Process Saf. Environ. Protect. 109 (2017) 63–71, https://doi.org/10.1016/j.psep.2017.03.032.

[35] D.S. S, V. Vishwakarma, Recovery and recycle of wastewater contaminated with heavy metals using adsorbents incorporated from waste resources and nanomaterials-A review, Chemosphere 273 (2021), https://doi.org/10.1016/j.chemosphere.2021.129677.

[36] Y. Gong, G. Liu, Q. Wang, A. Zhu, P. Liu, Q. Wu, Synthesis of a Novel Mesoporous Fe$_3$ O$_4$@SiO$_2$/CTAB-SiO$_2$ Composite Material and its Application in the Efficient Removal of Bisphenol A from Water, 2021, https://doi.org/10.1007/s00396-020-04801-6/.

[37] N. Li, F. Fu, J. Lu, Z. Ding, B. Tang, J. Pang, Facile preparation of magnetic mesoporous MnFe$_2$O$_4$@SiO$_2$−CTAB composites for Cr(VI) adsorption and reduction, Environ. Pollut. 220 (2017) 1376–1385, https://doi.org/10.1016/j.envpol.2016.10.097.

[38] E.T. Wahyuni, E.Z. Alharrisa, N.D. Lestari, S. Suherman, Modified waste polystyrene as a novel adsorbent for removal of methylene blue from aqueous media, Adv. Environ. Technol. 8 (2022) 83–92, https://doi.org/10.22104/AET.2022.5420.1465.

[39] S. Fadaei, M. Noorisepehr, H. Pourzamani, M. Salari, M. Moradnia, M. Darvishmotevalli, N. Mengelizadeh, Heterogeneous activation of peroxymonosulfate with Fe$_3$O$_4$ magnetic nanoparticles for degradation of Reactive Black 5: batch and column study, J. Environ. Chem. Eng. 9 (2021), https://doi.org/10.1016/j.jece.2021.105414.

[40] R. Roto, Y. Yusran, A. Kuncaka, Magnetic adsorbent of Fe$_3$O$_4$@SiO$_2$ core-shell nanoparticles modified with thiol group for chloroauric ion adsorption, Appl. Surf. Sci. 377 (2016) 30–36, https://doi.org/10.1016/j.apsusc.2016.03.099.

[41] A.K. Prabhakar, B.C. Mohan, M.H. Tai, Z. Yao, W. Su, S. Lay-Ming Teo, C.H. Wang, Green, non-toxic and efficient adsorbent from hazardous ash waste for the recovery of valuable metals and heavy metal removal from waste streams, Chemosphere 329 (2023), https://doi.org/10.1016/j.chemosphere.2023.138524.

[42] T.K.H. Ta, M.T. Trinh, N.V. Long, T.T.M. Nguyen, T.L.T. Nguyen, T.L. Thuoc, B.T. Phan, D. Mott, S. Maenosono, H. Tran-Van, V.H. Le, Synthesis and surface functionalization of Fe$_3$O$_4$-SiO$_2$ core-shell nanoparticles with 3-glycidoxypropyltrimethoxysilane and 1,1-carbonyldiimidazole for bio-applications, Colloids Surf. A Physicochem. Eng. Asp. 504 (2016) 376–383, https://doi.org/10.1016/j.colsurfa.2016.05.008.

[43] M.K. Seliem, M. Mobarak, Cr(VI) uptake by a new adsorbent of CTAB–modified carbonized coal: experimental and advanced statistical physics studies, J. Mol. Liq. 294 (2019), https://doi.org/10.1016/j.molliq.2019.111676.

[44] C.-W. Chen, T.-L. Yang, Y.-C. Chen, Using magnetic micelles as adsorbents to remove dyes from aqueous solutions, J. Environ. Chem. Eng. 11 (2023), 109457, https://doi.org/10.1016/j.jece.2023.109457.

[45] S.S. Kolluru, S. Agarwal, S. Sireesha, I. Sreedhar, S.R. Kale, Heavy metal removal from wastewater using nanomaterials-process and engineering aspects, Process Saf. Environ. Protect. 150 (2021) 323–355, https://doi.org/10.1016/j.psep.2021.04.025.

[46] N. Belachew, H. Hinsene, Preparation of cationic surfactant-modified kaolin for enhanced adsorption of hexavalent chromium from aqueous solution, Appl. Water Sci. 10 (2020), https://doi.org/10.1007/s13201-019-1121-7.

[47] L.M. Beleuk à Moungam, K.V. Tchieda, H. Mohamed, N.C. Pecheu, R.C. Kaze, E. Kamseu, A.D. Mvondo-Ze, I.K. Tonle, Efficiency of volcanic ash-based porous geopolymers for the removal of Pb^{2+}, Cd^{2+} and Hg^{2+} from aqueous solution, Cleaner Mater. 5 (2022), https://doi.org/10.1016/j.clema.2022.100106.

[48] T. Li, F. Zhu, W. Liang, H. Gu, X. Deng, Y. Xue, J. Guan, Simultaneous removal of p-nitrophenol and Cr(VI) using biochar supported green synthetic nano zero valent iron-copper: mechanistic insights and toxicity evaluation, Process Saf. Environ. Protect. 167 (2022) 629–640, https://doi.org/10.1016/j.psep.2022.09.049.

[49] Z. Fan, Q. Zhang, B. Gao, M. Li, C. Liu, Y. Qiu, Removal of hexavalent chromium by biochar supported nZVI composite: batch and fixed-bed column evaluations, mechanisms, and secondary contamination prevention, Chemosphere 217 (2019) 85–94, https://doi.org/10.1016/j.chemosphere.2018.11.009.

[50] S. Liang, W. Cai, C. Dang, X. Peng, Z. Luo, X. Wei, Synthesis of sodium alginate/phosphorus tetramethylmethyl sulfate biocomposite beads with exceptional adsorption rate for Cr(VI) removal, J. Environ. Chem. Eng. 11 (2023), https://doi.org/10.1016/j.jece.2023.109317.

[51] S.M.H. Asl, M. Ahmadi, M. Ghiasvand, A. Tardast, R. Katal, Artificial neural network (ANN) approach for modeling of Cr(VI) adsorption from aqueous solution by zeolite prepared from raw fly ash (ZFA), J. Ind. Eng. Chem. 19 (2013) 1044–1055, https://doi.org/10.1016/j.jiec.2012.12.001.

[52] M.K. Rai, G. Shahi, V. Meena, R. Meena, S. Chakraborty, R.S. Singh, B.N. Rai, Removal of hexavalent chromium Cr (VI) using activated carbon prepared from mango kernel activated with H_3PO_4, Resource-Efficient Technologies 2 (2016), https://doi.org/10.1016/j.reffit.2016.11.011. S63–S70.

[53] C. Santhosh, E. Daneshvar, K.M. Tripathi, P. Baltrėnas, T.Y. Kim, E. Baltrėnaitė, A. Bhatnagar, Synthesis and characterization of magnetic biochar adsorbents for the removal of Cr(VI) and Acid orange 7 dye from aqueous solution, Environ. Sci. Pollut. Control Ser. 27 (2020) 32874–32887, https://doi.org/10.1007/s11356-020-09275-1.

[54] M.A. Islam, M.J. Angove, D.W. Morton, Recent innovative research on chromium (VI) adsorption mechanism, Environ. Nanotechnol. Monit. Manag. 12 (2019), https://doi.org/10.1016/j.enmm.2019.100267.